Upregulated glucose metabolism correlates inversely with CD8+ T cell infiltration and survival in squamous cell carcinoma

Christian H. Ottensmeier[1], Kate L. Perry[1], Elena L. Harden[1], Jana Stasakova[1], Veronika Jenei[1], Jason Fleming[1], Oliver Wood[1], Jeongmin Woo[2], Christopher H. Woelk[2], Gareth J. Thomas[1,3], Stephen M. Thirdborough[1,3]

Cancer Sciences[1] and Clinical and Experimental Sciences[2], University of Southampton, Faculty of Medicine.

Running title: Correlates of T-cell infiltration in SCC

Keywords: Bioinformatics, TILs, GLUT-1, metabolism

Financial support: This study was funded by Cancer Research UK (C491/A15951).

Corresponding author: Stephen Thirdborough, University of Southampton, Cancer Sciences Unit, Somers Building MP824, Tremona Road, Southampton, SO16 6YD, UK.

Tel:(+44)2381205723

Email:s.m.thirdborough@soton.ac.uk

Figures and tables: 7 Figures (plus 5 Supplementary); 3 Supplementary Tables.

[3]Co-senior author

Abstract

Antibodies that block T cell regulatory checkpoints have recently emerged as a transformative approach to cancer treatment. However, the clinical efficacy of checkpoint blockade depends upon inherent tumor immunogenicity, with variation in infiltrating T cells contributing to differences in objective response rates. Here, we sought to understand the molecular correlates of tumor-infiltrating T lymphocytes (TIL) in squamous cell carcinoma (SCC), using a systems biologic approach to integrate publicly available omics datasets with histopathological features. We provide evidence that links TIL abundance and therapeutic outcome to the regulation of tumor glycolysis by EGFR and HIF, both of which are attractive molecular targets for use in combination with immunotherapeutics.

Introduction

The unprecedented success of antibodies against CTLA-4 and PD-1/PD-L1 has changed the landscape of cancer treatment (1). These mAb disrupt key molecular regulators on T-cells and boost anti-tumor immunity through the blockade of inhibitory signals (1). Unfortunately, only about a third of patients respond to checkpoint blocking antibodies, and currently there is no reliable way of identifying individuals most likely to benefit from immunotherapy.

Clinical trials of antibodies targeting the PD-1 pathway have demonstrated efficacy in tumors characterized by high TIL infiltration and expression of PD-L1 (2, 3), arguing that the clinical activity of checkpoint blockers is likely dependent on the presence of pre-existing T-cell responses subject to dominant immunosuppression. Numerous studies have reported that TIL frequency predicts for outcome (4), and we recently showed that this is true also for HPV-associated head and neck squamous cell carcinomas (HNSC) (5). Approximately 85% of HPV-positive HNSC contain a significant T-cell infiltrate suggesting that this tumor type is particularly immunologically visible. Unlike HPV-positive HNSC, most solid tumors contain widely varying levels of TILs and many immune escape mechanisms have been postulated to contribute to this. These include lack of chemokine-mediated trafficking (6), poor innate immune cell activation (7), and the presence of specific immunosuppressive populations, such as $Foxp3^+$ regulatory T-cells and myeloid-derived suppressor cells (8, 9).

To provide an unbiased global view of the underlying molecular processes that contribute to TIL frequency, we carried out a systems biological analysis of SCC data in The Cancer Genome Atlas (TCGA), involving weighted gene coexpression

network analysis (WGCNA) (10). Network analysis enables extraction of cell type-specific information from whole tissue whilst providing a system-level view and giving some insight into the communication between tumor, stroma and the host immune response. The power of WGCNA in capturing a systems perspective is built upon its underlying algorithm, which takes into account not only the correlation of two genes with each other but also the degree of similarity between a pair of genes in their correlation structure within the rest of the network (11). This strategy, applied to the analysis of SCC, identified inverse correlates of TIL infiltration that are associated with the natural evolution of cancer, encompassing genomic alterations and dysregulated signaling pathways that culminate in stabilization of HIF and elevated tumor glycolysis.

Materials and Methods

WGCNA

Raw read counts from SCC datasets, originating from head and neck, esophageal, cervical and lung tissues, were imported from TCGA into edgeR (12) and normalized using the limma-voom algorithm (13). Outlier subjects were identified and excluded using a sample network connectivity statistic described previously (14). WGCNA was performed on these pre-processed datasets, using the WGCNA package in R (10, 15). Networks were graphically depicted by exporting topological overlap weights into Gephi (http://gephi.org/) and the nodes clustered using ForceAtlas2. Functional enrichment of gene coexpression modules was evaluated by gene set enrichment analysis (GSEA) according to the pre-ranked protocol (http://www.broadinstitute.org/).

Survival analyses

The relationship between gene sets and patient survival outcomes was analyzed using Cox PH models. Specifically, patients were dichotomized according to high and low mean gene expression using cutoffs with a maximally selected log-rank statistic (Maxstat R function). Kaplan-Meier survival curves derived from the Cox PH model were then generated and differences between the two groups compared using the R survival package.

Immunohistochemistry

Tissue microarrays were constructed using triplicate, randomly selected, paraffin-embedded 1mm tumor cores (Aphelys Minicore 2, Mitogen). Automated immunostaining (Ventana XT) was performed by an accredited clinical pathology department using mAb against CD3, CD8 (Leica Microsystems), EGFR (Dako),

GLUT-1 and HIF-1α (Abcam). TILs were quantified using a Zeiss AxioCam MRc5 microscope and Zeiss Axiovision software (v4·8·1·0). An average intra-tumoral TIL score/high-power field was calculated across representative areas of each triplicate core. We have shown previously in this patient cohort that randomly selected triplicate TMA cores accurately reflect the heterogeneity of TIL infiltration within the tumor, and that TMA cell counts significantly correlate with whole-section TIL levels (5).

Cell culture and reagents

The TC-1 cell line, derived from transformed primary lung epithelial cells of C57BL/6 mice, and Phoenix Ecotropic cells were obtained from ATCC during 2011-2012, and not independently authenticated. Both cell lines were cultured in RPMI1640 supplemented with 10% FCS, 1mM sodium pyruvate, 2mM L-glutamine, 100units/mL penicillin, and 100μg/mL streptomycin (all Sigma-Aldrich). Cell lines were negative for *Mycoplasma* spp.

Retroviral transduction

The full-length cDNA for murine GLUT-1 was amplified by RT-PCR and cloned into pMSCV-puro (Clontech). Retroviral particles were generated in Phoenix Eco packaging cells, and transductants were selected with 2μg/ml puromycin (Sigma-Aldrich). To detect expression of GLUT-1, cells were fixed with methanol and then stained sequentially with anti-GLUT-1 (SPM498; Abcam) and FITC-conjugated goat anti-mouse IgG (Jackson ImmunoResearch Europe Ltd).

Analysis of cellular glycolysis

Experiments were performed using a Seahorse Bioscience XF96 Extracellular Flux Analyzer (North Billerica, MA, USA) in non-buffered DMEM (Sigma-Aldrich) supplemented with 1mM sodium pyruvate, 2mM L-glutamine at pH 7.4. Cells were seeded onto XF96 microplates on the day of the analysis, pre-coated with Cell-Tak (BD Biosciences), at a concentration of $4x10^4$ cells/well. Extracellular acidification rates were measured over time, during which glucose (0.5mM final concentration) and 2-DG (40mM final concentration) were injected.

Tumor therapy experiments

Female C57Bl/6 mice aged 6-8 weeks were injected subcutaneously with $5x10^5$ TC-1 cells transduced with pMSCV-puro or pMSCV-GLUT-1-puro into the dorsal flank. After 3 days, animals were subdivided into two further experimental groups, immunized with empty-vector or an E7/E6-encoding DNA vaccine, and tumor growth was followed over 3-weeks. Tumor volume was determined using the ellipsoidal volume formula: ½ x length x $width^2$. All animal experiments were performed according to UK Home Office guidelines (license number PPL 30/3028).

Statistical analysis

To assess differential gene expression between patient groups, either the non-parametric Wilcoxon signed-rank test or the Kruskal-Wallis test (for comparisons involving more than 2 groups) was performed. To correlate module eigengenes with binary traits, output p-values were –log10 transformed and given a sign according to whether the average rank was higher in the second (positive) or first (negative) group. These gene significance values were then correlated with the kME measure.

Results

The HNSC transcriptome is organized into consistent modules of coexpressed genes, which correspond to distinct biological processes

To identify gene signatures whose expression positively correlated with low TIL abundance, we applied WGCNA to a HNSC RNA-Seq dataset (16), publicly available via TCGA (Supplementary Fig. S1 provides an overview of the approach used in this study). The cohort analyzed consisted of tumors primarily from the oral cavity, larynx and oropharynx, and included both HPV-positive (n=34) and HPV-negative (n=212) cases. HPV-status was defined by mapping RNA-Seq reads to HPV genomes (16). After data pre-processing and outlier removal, a signed similarity matrix was built from pairwise correlations between gene expressions for the 4,000 most connected genes, ranked by the row sum of the adjacency matrix. Within this correlation matrix, 12 modules of highly coexpressed genes were identified by unsupervised hierarchical clustering on the basis of topological overlap (Fig. 1A). An index.html file that allows the network to be viewed and searched in a browser can be obtained from https://www.dropbox.com/sh/67xiyzz2wwn49pg/AAB1sIchHt9LYfscKUqIfnMxa?dl=0.

To establish whether the gene coexpression modules reflect distinct biological processes, Gene Ontology (GO) analyses were conducted in ToppGene (https://toppgene.cchmc.org/). All but one of the 12 modules had significant enrichment for at least one GO category, including processes linked to cancer such as M6 ‘cell cycle’, M3 ‘extracellular matrix organization’ and pertinent to our study, M1 ‘leukocyte activation’ and M8 ‘regulation of immune-system process’ (Table S1). A full list of GO categories is provided in Supplementary Table S2.

To determine if the network was reproducible across datasets, we evaluated whether module density and connectivity patterns defined in the RNA-Seq data were preserved in two independent HNSC cohorts (E-TABM-302, www.ebi.ac.uk/arrayexpress; http://bioinformatics.picr.man.ac.uk/vice/PublicProject.vice?pid=361) (17, 18). Of the 4,000 genes used to construct the aforementioned network, 3,557 (88.9%) were also present in the array data. Using network module preservation statistics (19), all modules except one (M5, corresponding to genes enriched for 'regulation of RNA metabolic process') were strongly preserved in the HNSC microarray data (Table S1), showing that gene coexpression modules are highly reproducible in HNSC. The lack of strong preservation of M5 is most likely due to the absence of 148 mapped RNA-Seq genes from M5 in the microarray probe sets, including the *C21orf62* hub gene.

Previously validated cluster analysis identified four subtypes of HNSC (basal, mesenchymal, classical and atypical), which are consistent with canonical genomic alterations (16, 20, 21). To capture the relationship between these transcriptional classes and the coexpression modules, we overlaid the TCGA-HNSC network (Fig. 1B) with the correlation between each gene's expression profile and the tumor subtype. This integrative approach revealed regions of the network showing changes in the HNSC transcriptome that correlated with a given subtype (Fig. 1C-F). Five modules (M3, M8, M11, M12 and border of M1) formed a network sub region ('meta-module') associated with mesenchymal tumors (Fig. 1C), which are defined by expression of genes linked with EMT and/or containing fibroblasts with a strong desmoplastic response (20). By contrast, the basal subtype, which typically exhibit *EGFR* and *MYC* gene amplification (21) and include tumors with *HRAS-CASP8* co-mutation (16), centered around modules M2 and M4 (Fig. 1D). The remaining

subtypes were associated with two further network regions, encompassing module M9 (classical, Fig. 1E) and modules M6, M5 and M1 (atypical, Fig. 1F). The classical subtype typically exhibits deletion of 3p and 9p, and amplification of 3q, whereas an enrichment of HPV-positive tumors and a lack of *EGFR* amplification or deletion of 9p characterize the atypical subtype (16, 21).

Coexpression modules are significantly associated with HNSC biomarkers

To study the relationships among identified modules and clinical variables, we summarized the expression profile of each module by its first principal component, termed the module eigengene (ME) (10), and correlated MEs with clinical traits and genetic alterations (Fig. 1G). This analysis highlighted modules associated with known HNSC biomarkers, including histopathological grade and TIL frequency, as well as HPV-status and EGFR gene amplification. Specifically, module M4 (GO:skin development) inversely correlated with tumor grade (corME4= -0.81). Consistent with this, examination of M4 revealed genes compatible with well-differentiated, keratinizing tumors, such as transglutaminase-1, involucrin and keratin-6B. Previous studies have reported an inverse correlation between EGFR expression and HPV-positive oropharyngeal cancers (22). Similarly, the MEs of M4 and M2 (GO:wound healing) were significantly associated with *EGFR* gene amplification (corME2=0.66; corME4=0.66) and inversely correlated with HPV-positivity (corME2= -0.78; corME4= -0.73). For M1, which had a strong reciprocal relationship with percent TILs (corME1=0.62), we also observed significant although opposite correlations with *EGFR* amplification (corME1= -0.55) and HPV-status (corME1=0.53), providing initial evidence of an inverse relationship between TILs and EGFR levels.

To investigate the relationship between genes inside modules and clinical outcome, we correlated gene expression with the deviance residual, a measure of observed minus expected hazard from univariate Cox regression analysis (23). Positive and negative values indicate shorter or longer than expected survival times, respectively. The corDeviance values were then correlated with a measure of module membership for each network gene (the kME measure) (10), defined by correlating its expression profile with the ME. Membership of four of the 12 modules (M1, M5, M8 and M11) was associated with good prognosis for overall survival (Supplementary Fig. S2A and S2B), whereas expression of modules M2, M3, M7 and M12 were associated with an unfavorable outcome.

The leukocyte activation module is enriched for genes associated with CD8$^+$ T-cells and overall survival

To characterize the cellular composition of the immune-related modules which correlated with TIL frequency, we mapped genes with the strongest membership for M1 (GO:leukocyte activation; kME1>0.80, 157 genes) (Fig. 2A) and M8 (GO:regulation of immune-system process; kME8>0.80, 150 genes) (Fig. 2B) to the coexpression atlas of the Immunological Genome Project (24). This analysis indicated that M1 was highly enriched for genes associated with CD8$^+$ TCR-αβ$^+$ T-cells (Bonferonni adj.P=4.0x10^{-47}), including components of the CD3-TCR complex (*CD3D*, *CD3E*, *CD3G* and *CD247*), chemokine receptors (*CCR5*, *CXCR3*) and cell adhesion molecules (*ITGAL*, *CD2*, *CD96*). In contrast, for M8, coexpression atlas mapping indicated enrichment for genes associated with cells of the myeloid lineage (adj.P=9.8x10^{-54}), including *CD14*, *CD163*, *MSR1* and *CSF1R*. The close topological proximity between M1 and M8 (Fig. 1B) suggests an interdependence and mutual

regulatory relationship between these two cell populations. It was noteworthy, that *VSIG4*, a strong negative regulator of T-cell proliferation and IL-2 production (25), was among the myeloid signature genes that correlated with a shorter than expected survival time (Fig. 2B). Thus, while increased expression of the $CD8^+$ T-cell signature was predictive of survival in both univariate and multivariate analyses (Supplementary Fig. S3A and C), no significant prognostic value was observed for the myeloid lineage gene set (Fig. S3B and C).

The interferon-signaling pathway is associated with chronically activated $CD8^+$ T-cells in HNSC

To further characterize the $CD8^+$ T-cell population, we tested whether the kME1≥ 0.8 gene set was enriched in the transcriptome of memory, effector and exhausted $CD8^+$ T-cells as defined by Wherry and colleagues in a model of acute versus chronic infection (GSE41867) (26). GSEA revealed that the genes were significantly over-represented in effector (day15) $CD8^+$ T-cells, responding to chronic (Fig. 3A) as opposed to acute LCMV infection (Fig. 3B). In this late anti-LCMV effector response, differentially expressed genes are exhaustion biased and reflect prolonged IFN-signaling (27). To examine whether this relationship extends to TILs in HNSC, we selected the nearest gene neighbors of *STAT1*, a key mediator of cellular responses to type-1 and -2 IFN, using an empirical topological overlap threshold of ≥0.07 (179 genes). Pathways common analysis in ToppGene indicated that this gene list was highly overrepresented in IFN-signaling genes (adj.$P=5.8\times10^{-46}$). Based on their kME, principal component analysis (PCA) separated the *STAT1* coexpressed genes into two distinct clusters corresponding to membership of M10 (GO:type-1 IFN-signaling pathway) or M1/M8 (GO:leukocyte activation/ regulation of immune-system process) (Fig. 3C). Within the latter were components of the CD3-TCR complex and *CD8A*, as

well as genes encoding $CD8^+$ T-cell effector molecules such as granzyme B, perforin-1, Fas ligand and IFN-γ. Additionally, 212 out of 751 M1 genes were identified as IFN-responsive in the Interferome database (28), suggesting that M1 reflects ongoing (chronic) T-cell-mediated inflammation. This premise was supported by the correlation of several inhibitory receptor genes, including *TIGIT*, *PDCD1* (PD-1), and *LAG3*, with *STAT1* and *CD8A* expression (Fig. 3C). Unsupervised hierarchical clustering of the nearest neighbor genes of *STAT1* failed to differentiate between HPV-status (Fig. 3D), indicating that $CD8^+$ T-cell responses were not necessarily directed toward viral antigens (29). Nevertheless, expression of multiple inhibitory receptor genes argues for an antigen-specific component to these responses and suggests these phenotypically exhausted T-cells are providing a level of tumor control, as proposed by Zehn and colleagues (30).

Expression of the leukocyte activation module inversely correlates with dysregulated tumor metabolism

The primary aim of this analysis was to identify gene sets from the HNSC network whose expression was associated with low TIL abundance. Towards this goal, we next focused on modules that inversely correlated with M1, namely modules M2, M4 and M7 (Fig. 4A), which together comprised a meta-module associated with basal tumors (Fig. 1D). Examination of genes with a strong membership of these modules (kME≥0.70) revealed GO categories enriched for wound healing, skin development and translational termination (Table S1). To understand the potential molecular basis by which these module genes regulate TIL frequency, we combined pathway analysis based on genes that inversely correlated with M1 (kME1< -0.40) followed by network visualization of enriched pathways using ToppCluster (31). This approach linked EGFR triggering with mTOR signaling and aerobic glycolysis (Supplementary

Fig. S4A). To further evaluate this association, GSEA was performed to characterize an extended network gene list (15,749 genes), pre-ranked by the correlation between the gene's expression profile and ME1. In agreement with the analysis in ToppCluster, GSEA showed that gene signatures of Myc activation, mTORC1 signaling and glycolysis were negatively correlated with membership of M1 (Fig. 4B-D, see also Table S2). Among the core-enriched genes recurring in these pathways were those coding for critical components of glucose and glutamine metabolism (Fig. 4E), such as facilitated glucose transporter, member 1 (GLUT-1; kME1= -0.57), fructose-biphosphate aldolase A (kME1= -0.45) and the terminal enzyme of glycolysis, pyruvate kinase (PKM2; kME1= -0.40). Consistent with the inverse correlation with M1, increased expression of this gene set is associated with decreased survival time (Supplementary Fig. S4B).

Expression of *HIF1A*, an important regulator of glycolysis (32), was significantly higher in basal tumors compared to the rest of the transcriptional subtypes (Fig. 4F) and inversely correlated with ME1 (r= -0.29). To examine the relationship between HIF1A target genes and the four transcriptional subtypes of HNSC, we correlated network gene expression and the first principal component of a hypoxia-associated gene set (33). The hypoxia eigengene highlighted regions of the network centered on module M2 (Fig. 4G), but also included elements of modules M3 (GO:extracellular matrix organization) and M10 (GO:type-1 IFN-signaling pathway). Taken together, these findings suggested that the strong inverse correlation with module M1 and basal subtype tumors could be due to increased glycolysis driven by hypoxia and/or EGFR signaling.

Of the 246 HNSC samples subjected to WGCNA, 171 had paired reverse-phase protein array (RPPA) data for 161 cancer-related proteins and phosphoproteins,

including EGFR. We therefore correlated protein expression from matched samples with the MEs. In accord with the RNA-Seq data, coexpression of proteins positively associated with ME2, ME4 and ME7, inversely correlated with ME1 (Fig. 5A-C). To investigate the relationship between these proteins and HIF1A activity, we overlaid a coexpression network constructed from the RPPA data with the correlation between each protein's expression profile and the M1 or hypoxia signature eigengene. This approach revealed a cluster of proteins positively correlated with HIF1A-responsive genes that inversely correlated with M1 (Fig. 5D). Among these proteins were phosphorylated HER2 (Y1248) and EGFR (Y992, Y1068 and Y1173).

The inverse relationship between a leukocyte activation module and tumor metabolism is a consistent feature of SCC

To explore how HIF1A activity and tumor metabolism affects the percentage of TILs in other types of SCC, we used consensus WGCNA to identify conserved modules across cervical (n=200), esophageal (n=83) and lung (n=362) RNA-Seq datasets. Full details of the resulting network (Fig. 6A) are provided in Table S3. All 17 consensus modules, which by construction are present in all input datasets (15), were also strongly preserved in the HNSC adjacency matrix (Table S3). Among the consensus modules was cM6 (GO:leukocyte activation), which significantly correlated with percent TILs ($r=0.43$, $p=8.9\times10^{-16}$) and for genes overrepresented in effector $CD8^+$ TCR-$\alpha\beta^+$ T-cells (adj.$P=7.6\times10^{-68}$). Expression of modules cM1 (GO:translational initiation), cM2 (GO:chromosome organization), cM7 (GO:xenobiotic metabolic process) and cM10 (GO:cell-cycle process) inversely correlated with cM6 (Table S3 and Fig. 6B), which together comprised a meta-module associated with HIF1A-responsive genes (Fig. 6C). The observed negative

correlation of cM6 (GO:leukocyte activation) with HIF1A activity (cor cME6= -0.37, $p=1.5x10^{-11}$) suggests that either the tumor tissue was hypoxic, or it featured activated receptor tyrosine kinase and/or PI3K/Akt/mTOR pathways that stabilize HIF1A (34, 35). Supporting the latter, GSEA showed that a hallmark gene signature of mTORC1 signaling was negatively associated with membership of cM6 (Fig. 6D). Among genes that inversely correlated with cM6 were those coding for EGFR, HER2 (ERBB2), Akt and components of mTORC1, including Raptor and mLST8 (Fig. 6E). The mTORC1 complex is a central regulator of cellular metabolism and promotes glycolysis by inducing PKM2 under normoxic conditions (36). Furthermore, expression of DEPTOR, a negative regulator of the MTOR signaling pathway, inversely correlated with the hypoxia eigengene whilst positively correlating with cM6 (Fig. 6E). Similarly, PTEN, which antagonizes PI3K function and consequently activation of Akt and PDK1 by dephosphorylating PIP_3, was among genes that positively correlated with cM6.

These findings are compatible with dysregulated signaling in SCC promoting HIF1A stabilization, avid glucose uptake via GLUT-1 and elevated glycolysis. This may in turn lead to competition for glucose creating a T-cell immunosuppressive tumor microenvironment (37). Alternatively, lactate, the end product of glycolysis may impair T-cell expansion (38). In this regard, monocarboxylate transporter type 1 (*SLC16A1*) was among HIF1A-responsive genes that inversely correlated with the leukocyte activation ME (Fig. 6E and 4E).

High GLUT-1 expression inversely correlates with TIL infiltration in HNSC and delays tumor regression in a pre-clinical model of T-cell-based therapy

To confirm the association of low TIL abundance with GLUT-1 expression, tumor tissue from 308 HNSC patients (HPV-negative=187; HPV-positive=121) were analyzed by immunohistochemistry. Expression of GLUT-1 inversely correlated with TIL levels ($r= -0.42$, $p<0.001$), as assessed on H&E-stained sections, and inversely correlated with numbers of $CD3^+$ T-cells ($r= -0.43$, $p<0.001$) and $CD8^+$ T-cells ($r= -0.40$, $p<0.001$). Similarly, expression of HIF-1α inversely correlated with TILs ($r= -0.49$, $p<0.001$).

Of the 308 patients included in the study, 108 were known to have died from HNSC. We have previously shown that TIL density predicts for survival in this cohort of patients (Fig. 7A) (5). There was a highly significant difference between the Kaplan-Meier curves for mortality according to GLUT-1 expression (Log rank $p<0.001$, Fig. 7B). The hazard ratios (HR) for high GLUT-1 expression indicated a 3.0-fold increase in HNSC mortality compared with low expression (HR=2.96[1.81-4.82], $p=0.006$). However, these associations were non-significant after multivariate analysis adjusted for major HNSC risk factors (age, stage, HPV-status and grade) and high GLUT-1 (HR=1.79[0.92-3.28], $p=0.197$). Consistent with the WGCNA, a significant correlation was present between GLUT-1 and EGFR protein expression ($r=0.21$, $p<0.001$).

To validate these observations, we examined expression of EGFR, HIF-1α, GLUT-1 and TIL in 34 cases of lung SCC (93 TMA cores) and found a similar significant ($p<0.001$) inverse correlation between $CD8^+$ TIL with EGFR ($r= -0.34$), HIF-1α ($r= -0.54$) and GLUT-1 ($r= -0.43$). EGFR expression positively correlated with GLUT-1 ($r=0.50$).

To examine whether high GLUT-1 expression impacts on immune evasion by tumors, we engineered the syngeneic TC-1 tumor model (39), which expresses HPV16 E6 and E7, to overexpress murine GLUT-1 (Fig. 7C). Initially, we measured the TC-1 cells extracellular acidification rate (ECAR) as a surrogate marker of glycolysis. A base-line measure of ECAR was obtained in glucose-free media; we then added glucose to assess glycolysis, and finally inhibited glucose metabolism by adding 2-deoxyglucose (2-DG). The injection of glucose caused an increase in ECAR in both control-transduced and GLUT-1-transduced TC-1 cells, with a significantly higher increase in TC-1 cells overexpressing GLUT-1 ($p<0.0001$, Fig. 7D). The subsequent injection of 2-DG decreased ECAR to basal levels. Thus, TC-1 cells transduced with GLUT-1 had a significantly higher glycolytic rate.

To explore whether increased glucose metabolism affects the therapeutic potential of tumor-specific T-cells, we challenged syngeneic mice with control-transduced or GLUT-1-transduced TC-1 cells, and on day 3, immunized the recipients with empty-vector or a protective HPV16 E7/E6 fusion gene vaccine. Immunization with this DNA vaccine elicits an effector $CD8^+$ T-cell response largely focused on the immunodominant H-$2D^b$-binding E7 epitope RAHYNIVTF (Supplementary Fig. S5). Tumors grew progressively in empty-vector immunized mice at comparable rates (Fig. 7E and 7F). However, whereas immunization with E7/E6 rapidly prevented tumor progression in mice challenged with control-transduced TC-1 cells (10/10 mice tumor-free by day 17, Fig. 7G), the overexpression of GLUT-1 significantly delayed tumor regression (4/10 mice tumor-free by day 21, Fig. 7H).

Discussion

In this study, we employed a systems biologic approach to integrate HNSC omics data with histopathological features in order to identify molecular correlates of TIL frequency. Our analysis identified a leukocyte activation module associated with effector $CD8^+$ T-cells and favorable prognosis, whose expression inversely correlates with a HIF metabolic transcriptome. Here, we have demonstrated for the first time, to our knowledge that tumors engineered to have a higher glycolytic rate are resistant to T-cell-based immunotherapy. Our data provide evidence that link TIL abundance and therapeutic outcome to the regulation of aerobic glycolysis by EGFR and HIF1A, which are attractive targets for the development of more effective immunotherapeutic strategies.

Network analysis of the HNSC transcriptome identified two modules correlated with TIL frequency, M1 and M8, which are significantly enriched for genes associated with $CD8^+$ TCR-$\alpha\beta^+$ T-cells and myeloid cells, respectively. The eigengenes for these two modules are strongly correlated (r=0.81). Despite their close topological proximity, the unsupervised assignment of differentially co-expressed genes into separate modules by WGCNA, reflecting their distinct underlying cell populations and activities, exemplifies the power of this approach to extract cell type-specific information from whole tissue and to elucidate regulatory circuits. Module M1 contains a large number of genes induced by IFN-γ, including *CIITA* and genes of the MHC class II-dependent antigen processing pathway, indicating that IFN-γ is upregulated and biologically available. Furthermore, within M1, genes co-expressed with *STAT1* such as *CD8A*, *IFNG*, *PRF1* and *GZMB*, are consistent with previous reports identifying $CD8^+$ T-cell signatures prognostic for survival (4). Perhaps

paradoxically, this favorable T-cell signature is associated with expression of multiple inhibitory receptor genes, including *TIGIT*, *PD-1* and *LAG3*, which are thought to be markers of terminally differentiated 'exhausted' T-cells (40).

The correlation of higher TIL frequency with favorable outcome is compatible with tumor antigen-specific T-cells providing an immune surveillance role after clinical intervention. Indeed, the therapeutic effects achieved by blocking PD-1 signaling strongly supports this premise. However, the prognostic significance of TILs may also reflect a distinct underlying tumor biology (41). Of the four previously validated gene expression subtypes of HNSC (20, 21), the presence of the T-cell activation signature positively correlates with atypical and mesenchymal transcriptional classes, suggesting that tumors belonging to these subtypes are more capable of eliciting a productive T-cell response. For the atypical subtype, which is characterized by an enrichment of HPV-positive tumors, this capacity may reflect activation of a non-tolerized, HPV-specific polyclonal $CD8^+$ T-cell repertoire (42). The increased immunogenicity of mesenchymal tumors may reflect their distinct mutational landscape (16), with dissimilarities in oncogenic drivers between subsets potentially influencing the magnitude of neoantigenic T-cell stimulation. Conversely, variances in oncogenic signaling may alter the ability of the host to mount an anti-tumor immune response (16). Accordingly, we observed a strong inverse correlation with module M1 and basal-subtype tumors, which are associated with *EGFR* and *MYC* gene amplification, and high levels of HIF signaling. As a consequence, genes encoding glucose and amino acid transporters, glycolytic enzymes, lactate dehydrogenase and pyruvate dehydrogenase kinase are strongly upregulated in basal as compared with mesenchymal tumors. These proteins act in concert to increase glucose metabolism and glucose dependency, such that in poorly

vascularized tumors, heightened glycolytic activity can lead to glucose depletion and accumulation of lactate (43). Activated T-cells use similar metabolic programs to support anabolic growth, proliferation and effector function (44), which implies tumor-infiltrating T-cells, may have to compete for metabolic fuels. Glucose deprivation or inhibition of glycolysis by 2-DG impairs cell cycle progression, production of IFN-γ, and granule-mediated cytotoxicity of $CD8^+$ T-cells (45-47). More recently, it has been shown that glucose deprivation leads to a reduction of the glycolysis metabolite phosphoenolpyruvate, which is required to sustain TCR-mediated Ca^{2+}-NFAT signaling and anti-tumor T-cell effector functions by repressing sarco/ER Ca^{2+}-ATPase activity [48]. Glucose limitation can also lead to increased expression of PD-1 (37), suggesting that competition for metabolites may precede T-cell dysfunction. In this regard, blockade of PD-1 has been recently shown to boost anti-tumor $CD8^+$ T-cell responses by augmenting their glycolytic capacity through increased mTOR signaling and glucose flux (49).

Our data suggest that targeting the EGFR pathway might offer a means of selectively modulating tumor metabolism, as reported in lung adenocarcinoma cells (50), without disrupting T-cell effector function. Trials, which combine standard treatment of anti-EGFR (Cetuximab) and chemotherapy with anti-PD-1 (Pembrolizumab), are already ongoing in metastatic or recurrent HNSC (e.g., NCT02358031). In future work, it will therefore be of interest to evaluate whether molecular predictors of outcome can be confirmed in interventional trials.

Acknowledgements

We are grateful to the UoS BRF for support with animal work. Drs Agnete Fredriksen and Ole Brekke (Vaccibody, Oslo, Norway) kindly provided the E7/E6 DNA vaccine.

References

1. Wolchok JD, and Chan TA. Cancer: Antitumour immunity gets a boost. Nature 2014;515:496-8.

2. Herbst RS, Soria JC, Kowanetz M, Fine GD, Hamid O, Gordon MS, et al. Predictive correlates of response to the anti-PD-L1 antibody MPDL3280A in cancer patients. Nature 2014;515:563-7.

3. Tumeh PC, Harview CL, Yearley JH, Shintaku IP, Taylor EJ, Robert L, et al. PD-1 blockade induces responses by inhibiting adaptive immune resistance. Nature 2014;515:568-71.

4. Galon J, Angell HK, Bedognetti D, Marincola FM. The continuum of cancer immunosurveillance: prognostic, predictive, and mechanistic signatures. Immunity 2013;39:11-26.

5. Ward MJ, Thirdborough SM, Mellows T, Riley C, Harris S, Suchak K, et al. Tumour-infiltrating lymphocytes predict for outcome in HPV-positive oropharyngeal cancer. Br J Cancer 2014;110:489-500.

6. Harlin H, Meng Y, Peterson AC, Zha Y, Tretiakova M, Slingluff C, et al. Chemokine expression in melanoma metastases associated with CD8+ T-cell recruitment. Cancer Res 2009;69:3077-85.

7. Fuertes MB, Kacha AK, Kline J, Woo SR, Kranz DM, Murphy KM, Gajewski TF. Host type I IFN signals are required for antitumor CD8+ T cell responses through CD8{alpha}+ dendritic cells. J Exp Med 2011;208:2005-16.

8. Gabrilovich DI, Ostrand-Rosenberg S, Bronte V. Coordinated regulation of myeloid cells by tumours. Nat Rev Immunol 2012;12:253-68.

9. Nomura T, and Sakaguchi S. Naturally arising CD25+CD4+ regulatory T cells in tumor immunity. Curr Top Microbiol Immunol 2005;293:287-302.

10. Langfelder P, and Horvath S. WGCNA: an R package for weighted correlation network analysis. BMC Bioinformatics 2008;9:559.

11. Gaiteri C, Ding Y, French B, Tseng GC, Sibille E. Beyond modules and hubs: the potential of gene coexpression networks for investigating molecular mechanisms of complex brain disorders. Genes Brain Behav 2014;13:13-24.

12. Robinson MD, McCarthy DJ, Smyth GK. edgeR: a Bioconductor package for differential expression analysis of digital gene expression data. Bioinformatics 2010;26:139-40.

13. Ritchie ME, Phipson B, Wu D, Hu Y, Law CW, Shi W, Smyth GK. limma powers differential expression analyses for RNA-sequencing and microarray studies. Nucleic Acids Res 2015;43:e47.

14. Oldham MC, Langfelder P, Horvath S. Network methods for describing sample relationships in genomic datasets: application to Huntington's disease. BMC Syst Biol 2012;6:63.

15. Langfelder P, Mischel PS, Horvath S. When is hub gene selection better than standard meta-analysis? PLoS One. 2013;8:e61505.

16. Comprehensive genomic characterization of head and neck squamous cell carcinomas. Nature 2015;517:576-82.

17. Rickman DS, Millon R, De Reynies A, Thomas E, Wasylyk C, Muller D, et al. Prediction of future metastasis and molecular characterization of head and neck squamous-cell carcinoma based on transcriptome and genome analysis by microarrays. Oncogene 2008;27:6607-22.

18. Thurlow JK, Pena Murillo CL, Hunter KD, Buffa FM, Patiar S, Betts G, et al. Spectral clustering of microarray data elucidates the roles of microenvironment remodeling and immune responses in survival of head and neck squamous cell carcinoma. J Clin Oncol 2010;28:2881-8.

19. Langfelder P, Luo R, Oldham MC, Horvath S. Is my network module preserved and reproducible? PLoS Comput Biol 2011;7:e1001057.

20. Chung CH, Parker JS, Karaca G, Wu J, Funkhouser WK, Moore D, et al. Molecular classification of head and neck squamous cell carcinomas using patterns of gene expression. Cancer Cell 2004;5:489-500.

21. Walter V, Yin X, Wilkerson MD, Cabanski CR, Zhao N, Du Y, et al. Molecular subtypes in head and neck cancer exhibit distinct patterns of chromosomal gain and loss of canonical cancer genes. PloS One 2013;8:e56823.

22. Reimers N, Kasper HU, Weissenborn SJ, Stutzer H, Preuss SF, Hoffmann TK, et al. Combined analysis of HPV-DNA, p16 and EGFR expression to predict prognosis in oropharyngeal cancer. Int J Cancer 2007;120:1731-8.

23. Therneau TM, Grambsch PM, Fleming TR. Martingale-based residuals for survival models. Biometrika 1990;77:147-60.

24. Heng TS, and Painter MW. The Immunological Genome Project: networks of gene expression in immune cells. Nat Immunol 2008;9:1091-4.

25. Vogt L, Schmitz N, Kurrer MO, Bauer M, Hinton HI, Behnke S, et al. VSIG4, a B7 family-related protein, is a negative regulator of T cell activation. J Clin Invest 2006;116:2817-26.

26. Doering TA, Crawford A, Angelosanto JM, Paley MA, Ziegler CG, Wherry EJ. Network analysis reveals centrally connected genes and pathways involved in CD8+ T cell exhaustion versus memory. Immunity 2012;37:1130-44.

27. Crawford A, Angelosanto JM, Kao C, Doering TA, Odorizzi PM, Barnett BE, et al. Molecular and transcriptional basis of CD4(+) T cell dysfunction during chronic infection. Immunity 2014;40:289-302.

28. Rusinova I, Forster S, Yu S, Kannan A, Masse M, Cumming H, et al. Interferome v2.0: an updated database of annotated interferon-regulated genes. Nucleic Acids Res 2013;41(Database issue):D1040-6.

29. Rooney MS, Shukla SA, Wu CJ, Getz G, Hacohen N. Molecular and genetic properties of tumors associated with local immune cytolytic activity. Cell 2015;160:48-61.

30. Speiser DE, Utzschneider DT, Oberle SG, Munz C, Romero P, Zehn D. T cell differentiation in chronic infection and cancer: functional adaptation or exhaustion? Nat Rev Immunol 2014;14:768-74.

31. Kaimal V, Bardes EE, Tabar SC, Jegga AG, Aronow BJ. ToppCluster: a multiple gene list feature analyzer for comparative enrichment clustering and network-based dissection of biological systems. Nucleic Acids Res 2010;38(Web Server issue):W96-102.

32. Semenza GL, Roth PH, Fang HM, Wang GL. Transcriptional regulation of genes encoding glycolytic enzymes by hypoxia-inducible factor 1. J Biol Chem 1994;269:23757-63.

33. Buffa FM, Harris AL, West CM, Miller CJ. Large meta-analysis of multiple cancers reveals a common, compact and highly prognostic hypoxia metagene. Br J Cancer 2010;102:428-35.

34. Laughner E, Taghavi P, Chiles K, Mahon PC, Semenza GL. HER2 (neu) signaling increases the rate of hypoxia-inducible factor 1alpha (HIF-1alpha) synthesis: novel mechanism for HIF-1-mediated vascular endothelial growth factor expression. Mol Cell Biol 2001;21:3995-4004.

35. Zhong H, Chiles K, Feldser D, Laughner E, Hanrahan C, Georgescu MM, et al. Modulation of hypoxia-inducible factor 1alpha expression by the epidermal growth factor/phosphatidylinositol 3-kinase/PTEN/AKT/FRAP pathway in human prostate cancer cells: implications for tumor angiogenesis and therapeutics. Cancer Res 2000;60:1541-5.

36. Sun Q, Chen X, Ma J, Peng H, Wang F, Zha X, et al. Mammalian target of rapamycin up-regulation of pyruvate kinase isoenzyme type M2 is critical for aerobic glycolysis and tumor growth. Proc Natl Acad Sci USA 2011;108:4129-34.

37. Chang CH, Curtis JD, Maggi LB Jr, Faubert B, Villarino AV, O'Sullivan D, et al. Posttranscriptional control of T cell effector function by aerobic glycolysis. Cell 2013;153:1239-51.

38. Droge W, Roth S, Altmann A, Mihm S. Regulation of T-cell functions by L-lactate. Cell Immunol 1987;108:405-16.

39. Lin KY, Guarnieri FG, Staveley-O'Carroll KF, Levitsky HI, August JT, Pardoll DM, et al. Treatment of established tumors with a novel vaccine that enhances major histocompatibility class II presentation of tumor antigen. Cancer Res 1996;56:21-6.

40. Virgin HW, Wherry EJ, Ahmed R. Redefining chronic viral infection. Cell 2009;138:30-50.

41. Kostareli E, Holzinger D, Bogatyrova O, Hielscher T, Wichmann G, Keck M, et al. HPV-related methylation signature predicts survival in oropharyngeal squamous cell carcinomas. J Clin Invest 2013;123:2488-501.

42. Albers A, Abe K, Hunt J, Wang J, Lopez-Albaitero A, Schaefer C, et al. Antitumor activity of human papillomavirus type 16 E7-specific T cells against virally infected squamous cell carcinoma of the head and neck. Cancer Res 2005;65:11146-55.

43. Schroeder T, Yuan H, Viglianti BL, Peltz C, Asopa S, Vujaskovic Z, et al. Spatial heterogeneity and oxygen dependence of glucose consumption in R3230Ac and fibrosarcomas of the Fischer 344 rat. Cancer Res 2005;65:5163-71.

44. Wang R, and Green DR. Metabolic checkpoints in activated T cells. Nat Immunol 2012;13:907-15.

45. Cham CM, and Gajewski TF. Glucose availability regulates IFN-gamma production and p70S6 kinase activation in $CD8^+$ effector T cells. J Immunol 2005;174:4670-7.

46. Cham CM, Driessens G, O'Keefe JP, Gajewski TF. Glucose deprivation inhibits multiple key gene expression events and effector functions in $CD8^+$ T cells. Eur J Immunol 2008;38:2438-50.

47. Jacobs SR, Herman CE, Maciver NJ, Wofford JA, Wieman HL, Hammen JJ, et al. Glucose uptake is limiting in T cell activation and requires CD28-mediated Akt-dependent and independent pathways. J Immunol 2008;180:4476-86.

48. Ho PC, Bihuniak JD, Macintyre AN, Staron M, Liu X, Amezquita R, et al. Phosphoenolpyruvate is a metabolic checkpoint of anti-tumor T-Cell responses. Cell 2015;162:1217-28.

49. Chang CH, Qiu J, O'Sullivan D, Buck MD, Noguchi T, Curtis JD, et al. Metabolic competition in the tumor microenvironment is a driver of cancer progression. Cell 2015;162:1229-41.

50. Makinoshima H, Takita M, Matsumoto S, Yagishita A, Owada S, Esumi H, et al. Epidermal growth factor receptor (EGFR) signaling regulates global metabolic pathways in EGFR-mutated lung adenocarcinoma. J Biol Chem 2014;289:20813-23.

Figure 1. Gene coexpression and eigengene relationships with HNSC transcriptional subclasses and clinico-pathological features. (A) Hierarchical clustering dendrogram for all 4000 genes used in the analysis. The color row underneath the dendrogram shows the module assignment. (B) Network graph where each node represents a gene labelled by color according to the module assignment in (A). Distance between nodes is represented by the topological overlap connectivity measure. (C-F) Network graphs where each gene is labelled by color according to correlation with the indicated HNSC tumor subtype. Red and blue colors show positive and negative correlation, respectively. (G) Heat map of the correlation between expression of each ME and the clinical trait listed. Abbreviations: ECS (extracapsular spread), LVI (lymphovascular invasion), PNI (perinuclear invasion).

Figure 2. Analysis of immune-related module gene expression and eigengene relationships with overall survival. Scatterplots between module membership (kME) and a prognostic gene significance measure (corDeviance) for genes with the strongest membership (kME≥0.8) for M1 (A) and M8 (B).

Figure 3. The IFN-signaling pathway is associated with chronically activated CD8$^+$ T-cells in HNSC. (A and B) GSEA of microarray data from purified CD8$^+$ T-cells at day 15 of chronic (A) or acute (B) LCMV infection, using a gene set representing the strongest members of M1 (kME1≥0.8). (C) PCA of the nearest neighbor genes of *STAT1*. Genes are colored according to membership of M1 (turquoise), M8 (pink) and M10 (purple). The PCA plot is overlaid with the corresponding variables factor graph, where the angle between two arrows represents the correlation of the respective MEs. Arrows directly opposite are negatively correlated. (D) Unsupervised hierarchical clustering based on the nearest neighbor genes of *STAT1*. Each row represents a gene, each column a sample from

HPV-positive (green) or HPV-negative (blue) patients, and each cell the expression level of a gene in a sample using a color scale where red indicates overexpression and blue underexpression relative to mean expression in each row.

Figure 4. Expression of the leukocyte activation module inversely correlates with tumor glycolysis. (A) Heat map of the correlation between expression of each ME; cells show correlation coefficient (top) and corresponding p-value (bottom). (B-D) GSEA of HNSC genes pre-ranked by membership of M1 (high-to-low) with given MSigDB Hallmark gene sets. A negative NES indicates gene set enrichment at the bottom of the ranked list. (E) Bar graph of a glucose metabolism gene set (x-axis) with correlation between the gene's expression profile and membership of the module indicated. (F) *HIF1A* $\log_2$ expression. Each data point represents a tumor sample classified according to the transcriptional subtype indicated. (G) Network gene correlation with a hypoxia signature eigengene. Red and blue colors show positive and negative correlation, respectively.

Figure 5. Proteins whose expression inversely correlate with M1 are associated with a hypoxia signature. (A-C) Scatterplots of correlations between expressions for the 161 cancer-related proteins and phosphoproteins in the HNSC RPPA data set with ME1 (x-axes) versus ME2 (A), ME4 (B) or ME7 (C). (D) Network graph where each node represents a protein labelled by color according to the correlation between its expression profile and ME1. Red and blue colors show positive and negative ME1 correlation, respectively. Node size reflects the strength of correlation with the hypoxia signature eigengene (larger size=stronger correlation).

Figure 6. Expression of a consensus leukocyte activation module inversely correlates with tumor glycolysis in SCC. Consensus SCC network graph where

nodes are labelled by color according to WGCNA module assignment (A) or correlation between the genes expression profile and cME6 (B) or a hypoxia signature eigengene (C). (D) GSEA of expressed genes (n=14,639) in SCC pre-ranked by membership of cM6 (high-to-low) with a mTORC1 hallmark gene set. (E) Scatterplot of a glucose metabolism gene set with correlation between the gene's expression profile and membership of the leukocyte activation module (x-axis) or a hypoxia-associated signature eigengene (y-axis). Meta-values were calculated by combining the Z scores of correlations from each dataset divided by the square root of the number of sets. Label size reflects the strength of correlation with cME6 (larger size=stronger negative correlation).

Figure 7. High GLUT-1 expression is predictive of poor outcome in HNSC and renders TC-1 tumors resistant to vaccine-induced T-cell-based therapy. (A and B) Kaplan-Meier curves for HNSC mortality according to abundance of TILs (A) or GLUT-1 expression (B). HNSC-specific survival time was measured from date of diagnosis until date of death from HNSC or date last seen alive. For those that died of other causes, survival from HNSC was censored at the time of death. (C) Histogram plot of GLUT-1 expression by control-transduced (green) or GLUT-1-transduced (purple) TC-1 cells. (D) Analysis of ECAR by control-transduced or GLUT-1-transduced TC-1 cells upon addition of glucose and 2-DG. (E-H) Tumor therapy experiments where syngeneic mice were injected subcutaneously with either control-transduced (E and G) or GLUT-1-transduced (F and H) TC-1 cells, and then 3-days later vaccinated with empty vector (E and F) or a DNA vaccine encoding E6/E7 (G and H). The data are representative of two independent experiments.

Figure 1

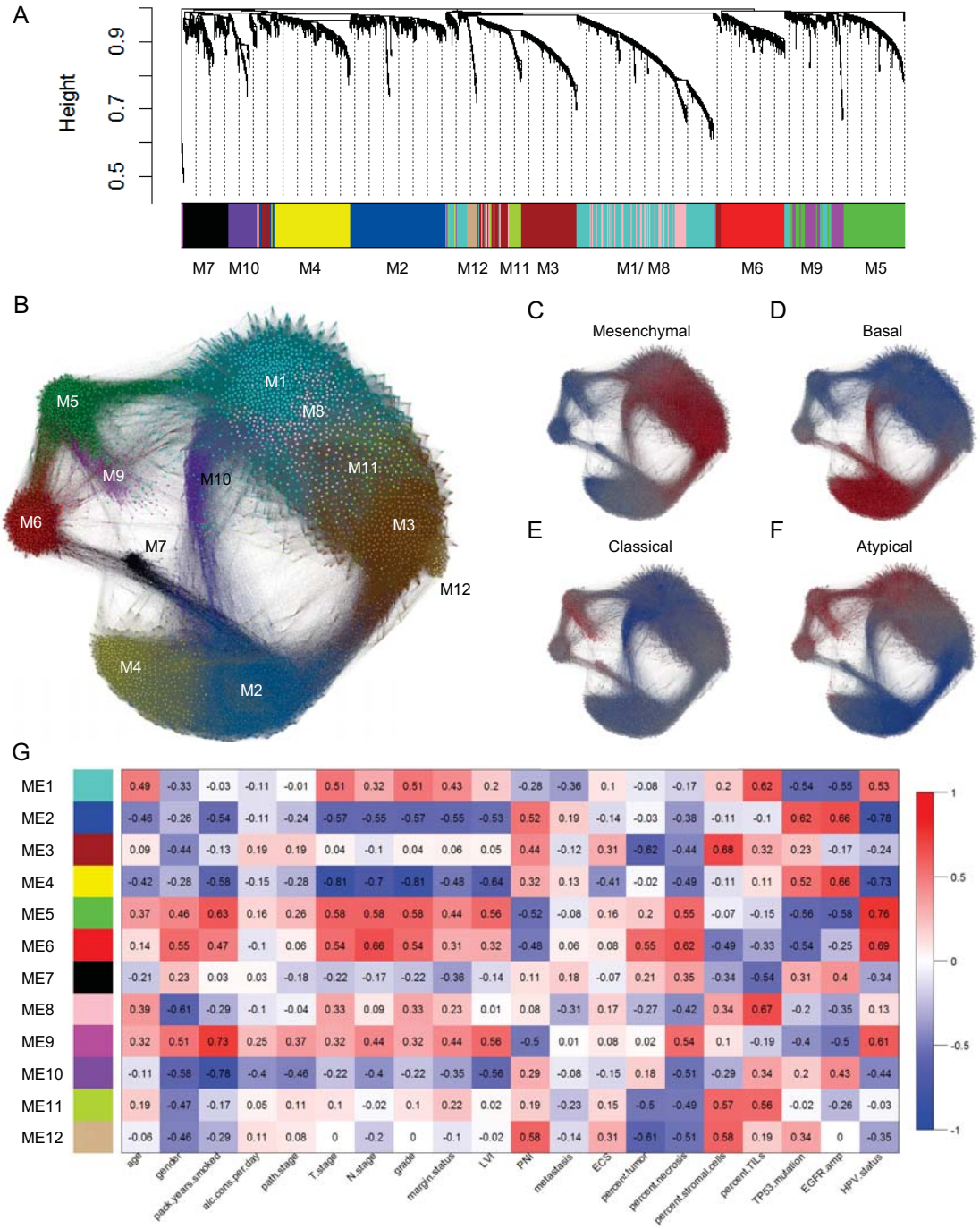

Figure 2

A

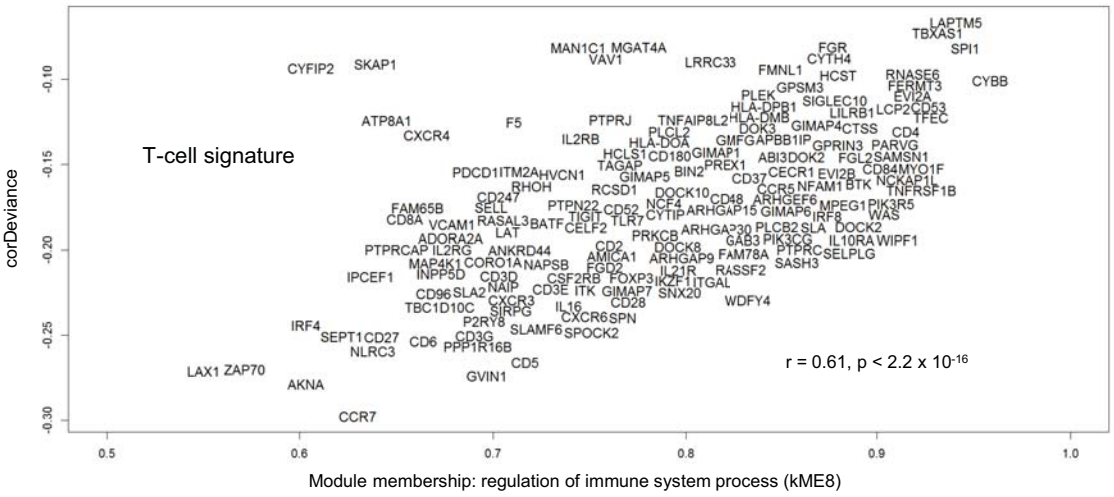

B

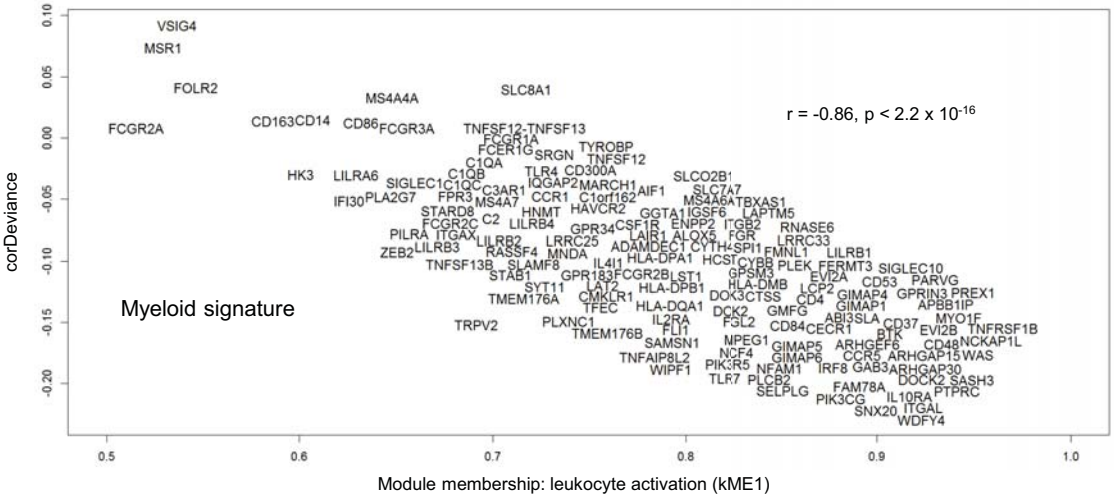

Author Manuscript Published OnlineFirst on May 20, 2016; DOI: 10.1158/0008-5472.CAN-15-3121
Author manuscripts have been peer reviewed and accepted for publication but have not yet been edited.

Figure 3

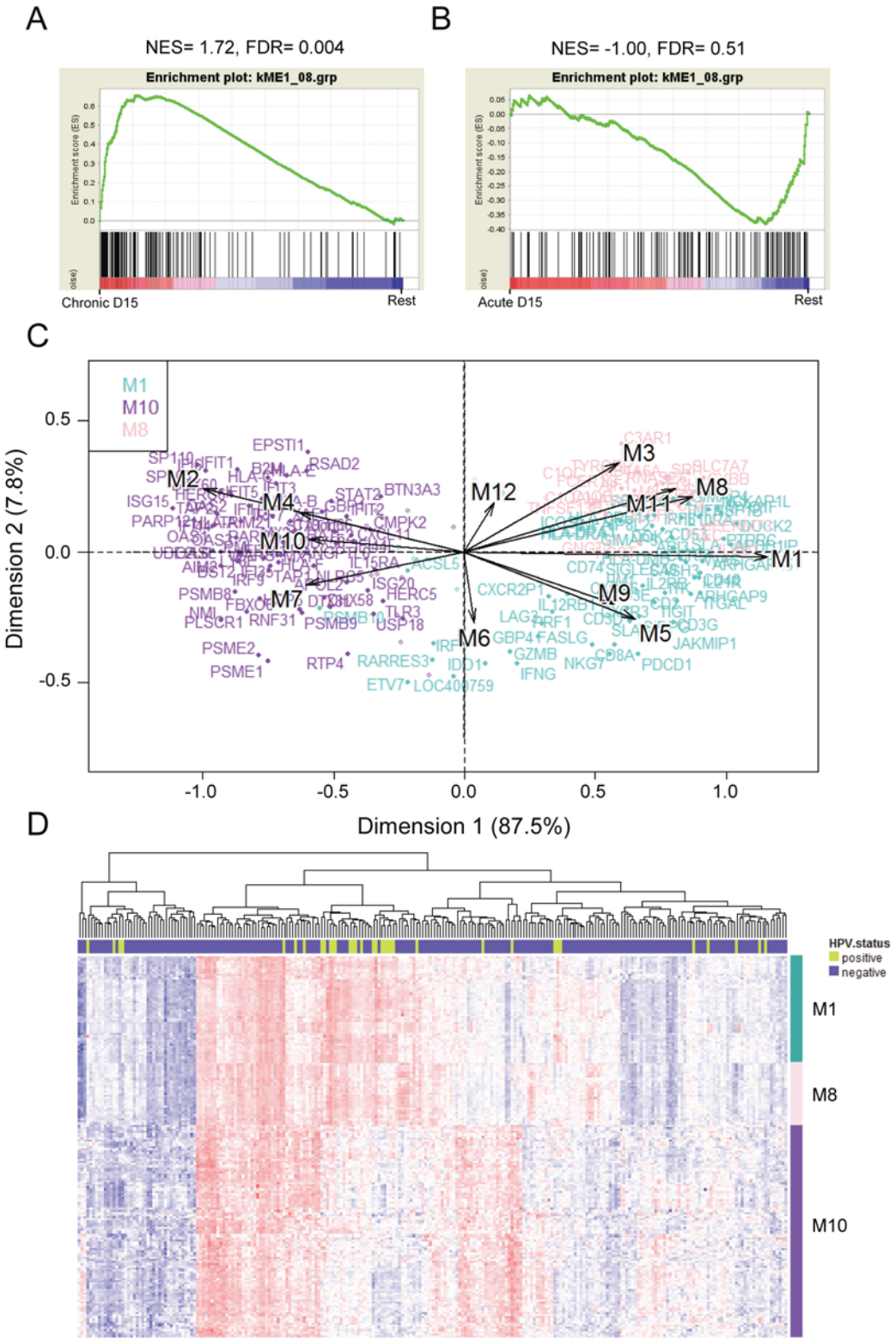

Author Manuscript Published OnlineFirst on May 20, 2016; DOI: 10.1158/0008-5472.CAN-15-3121
Author manuscripts have been peer reviewed and accepted for publication but have not yet been edited.

Figure 4

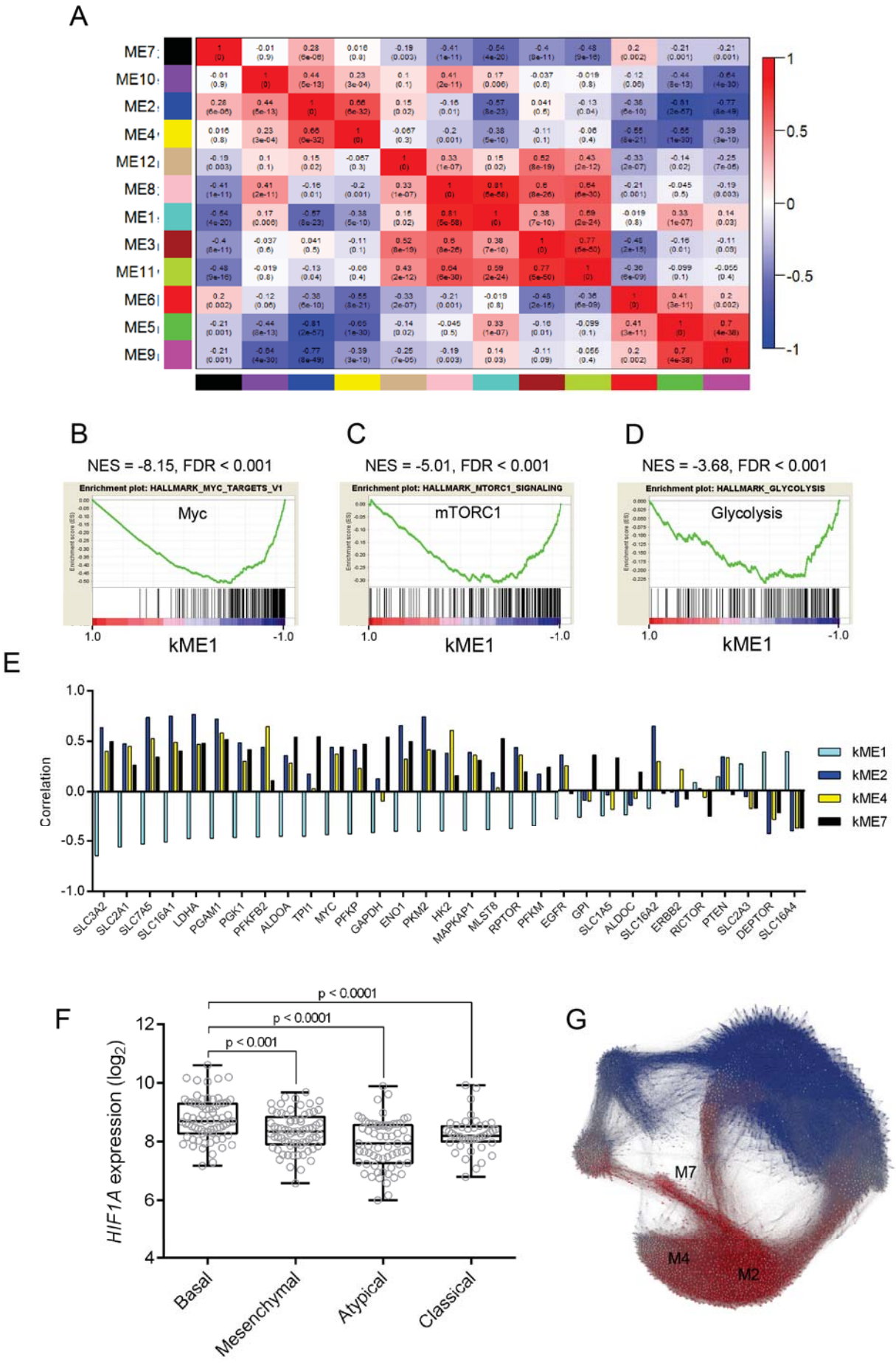

Author Manuscript Published OnlineFirst on May 20, 2016; DOI: 10.1158/0008-5472.CAN-15-3121
Author manuscripts have been peer reviewed and accepted for publication but have not yet been edited.

Figure 5

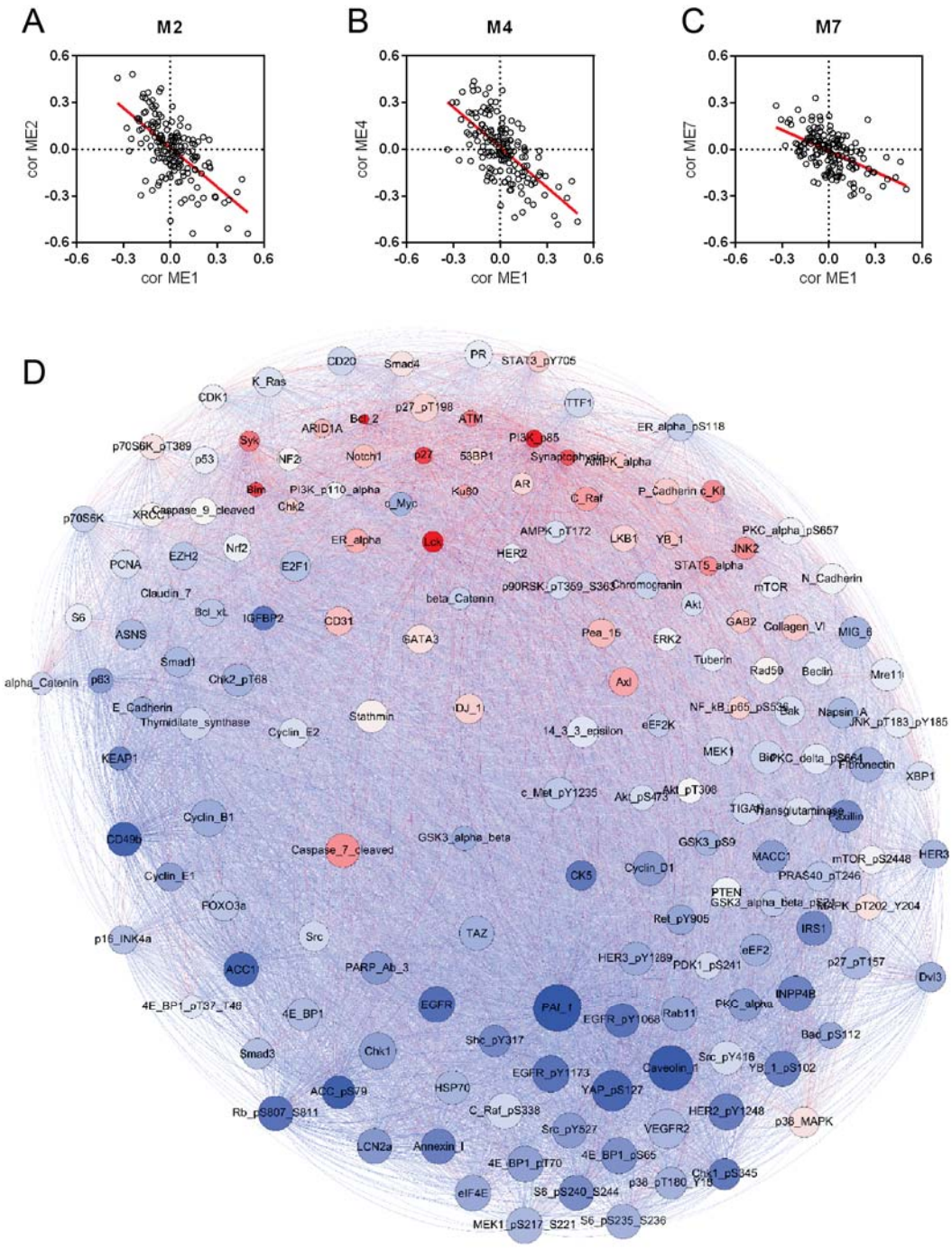

Author Manuscript Published OnlineFirst on May 20, 2016; DOI: 10.1158/0008-5472.CAN-15-3121
Author manuscripts have been peer reviewed and accepted for publication but have not yet been edited.

Figure 6

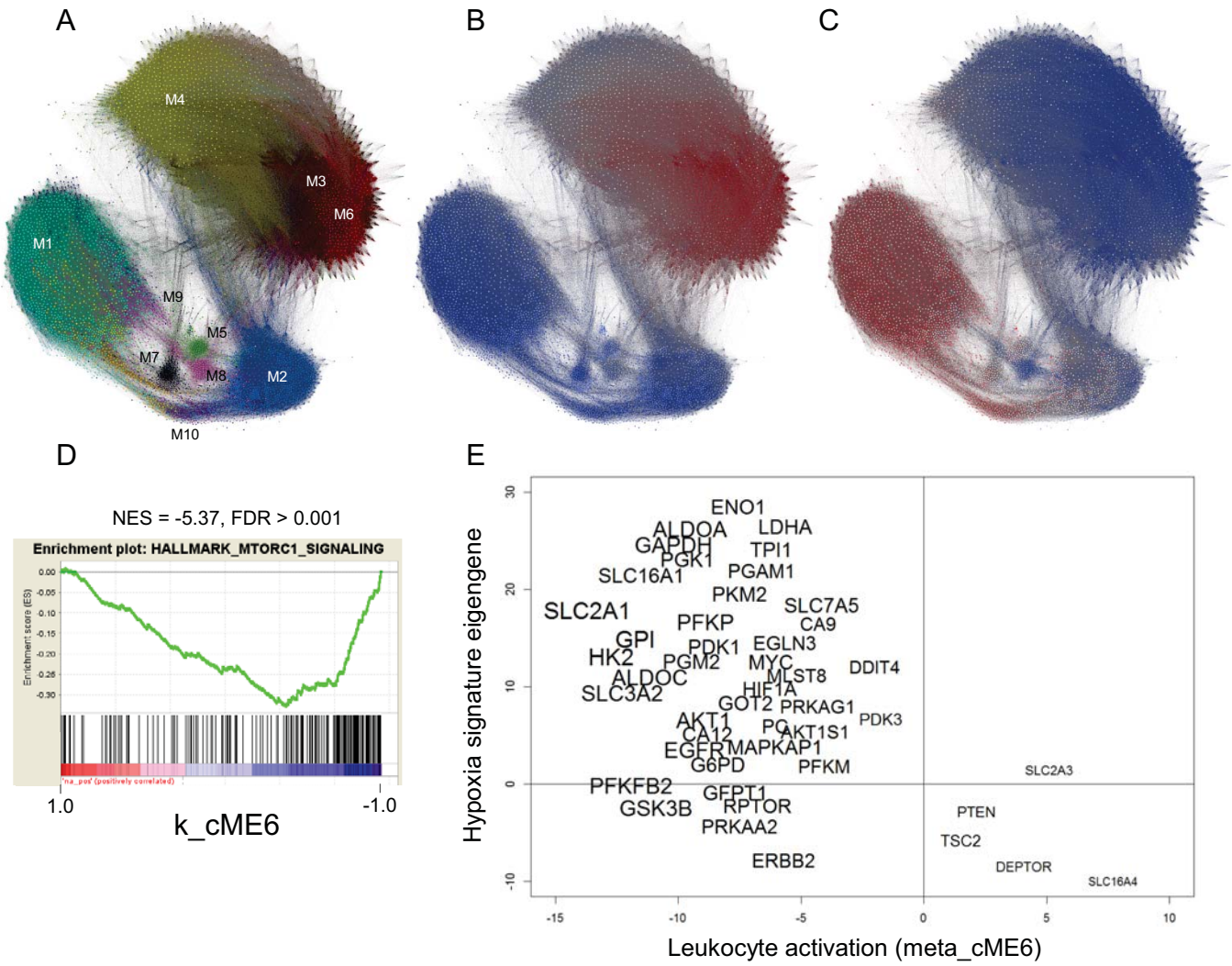

Figure 7

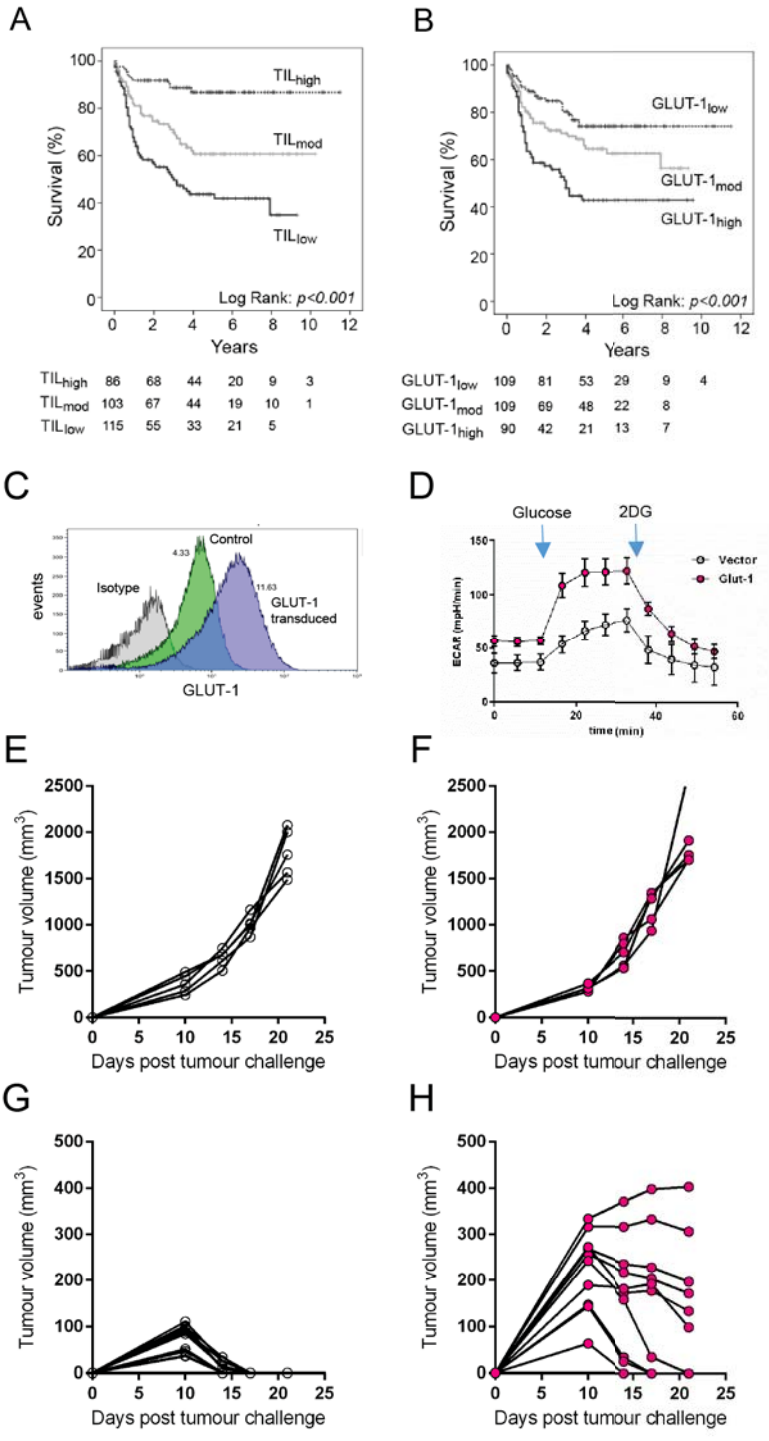

Cancer Research
The Journal of Cancer Research (1916–1930) | The American Journal of Cancer (1931–1940)

AACR American Association for Cancer Research

Upregulated glucose metabolism correlates inversely with CD8+ T cell infiltration and survival in squamous cell carcinoma

Christian H Ottensmeier, Kate L Perry, Elena L Harden, et al.

Cancer Res Published OnlineFirst May 20, 2016.